Geophysical Journal International

Geophys. J. Int. (2013) doi: 10.1093/gji/ggt043

Geophysical Journal International Advance Access published April 16, 2013

Depth sensitivity of seismic coda waves to velocity perturbations in an elastic heterogeneous medium

Anne Obermann,[1] Thomas Planès,[1] Eric Larose,[1] Christoph Sens-Schönfelder[1,2] and Michel Campillo[1]

[1] *ISTerre, CNRS, Université de Grenoble,* 38041 *Grenoble, France. E-mail: Anne.Obermann@ujf-grenoble.fr*
[2] *GFZ German Research Centre for Geosciences,* 14473 *Potsdam, Germany*

Accepted 2013 January 1. Received 2013 January 9; in original form 2012 August 22

SUMMARY

Numerous monitoring applications make use of seismic coda waves to evaluate velocity changes in the Earth. This raises the question of the spatial sensitivity of coda wave-based measurements. Here, we investigate the depth sensitivity of coda waves to local velocity perturbations using 2-D numerical wavefield simulations. We calculate the impulse response at the surface before and after a slight perturbation of the velocity within a thin layer at depth is introduced. We perform a parametric analysis of the observed apparent relative velocity changes, ε^{obs}, versus the depth of the thin perturbed layer. Through the analysis of the decay of ε^{obs}, we can discriminate two different regimes: one for a shallow perturbation and the other for a deep perturbation. We interpret the first regime as the footprint of the 1-D depth sensitivity of the fundamental surface wave mode. To interpret the second regime, we need to model the sensitivity of the multiply scattered body waves in the bulk. We show that the depth sensitivity of coda waves can be modelled as a combination of bulk wave sensitivity and surface wave sensitivity. The transition between these two regimes is governed by mode conversions due to scattering. We indicate the importance of surface waves for the sensitivity of coda waves at shallow depths and at early times in the coda. At later times, bulk waves clearly dominate the depth sensitivity and offer the possibility of monitoring changes at depths below the sensitivity of the surface waves. Based on the transition between the two regimes, we can discriminate a change that occurs at the surface from a change that occurs at depth. This is illustrated for shallow depth perturbations through an example from lunar data.

Key words: Coda waves; Computational seismology; Wave scattering and diffraction.

1 INTRODUCTION

Detecting slight temporal changes in elastic properties of rocks at depth is of increasing interest for various applications (Poupinet *et al.* 1984, 1996; Meunier *et al.* 2001; Snieder & Hagerty 2004; Niu *et al.* 2008). Provided that the sources and receivers are perfectly reproducible, the change in the seismic waveforms between two acquisitions performed at two distant dates can be solely attributed to changes in the propagation medium. When the medium is not too heterogeneous, locating such changes with ballistic waves is possible, although the sensitivity to weak changes is low. In contrast, in a highly heterogeneous medium, waves enter the multiple scattering regime. Heterogeneities in the medium generate late-arriving wave trains, which constitute the so-called 'coda'. These waves provide dense sampling of the medium and are very sensitive to small velocity perturbations. In optics, this sensitivity is used in diffuse wave spectroscopy (Pine *et al.* 1988). It is also used with elastic and acoustic waves in diffuse acoustic wave spectroscopy (Cowan *et al.* 2002) and with coda seismic (Poupinet *et al.* 1984; Snieder *et al.* 2002; Snieder 2006).

The detection of temporal changes has been successfully applied to different areas in seismology. These areas include the monitoring of oil reservoirs (Meunier *et al.* 2001), volcanoes (Grêt *et al.* 2005; Brenguier *et al.* 2008a), fault zones (Brenguier *et al.* 2008b), landslides (Mainsant *et al.* 2012) and even subduction zones (Rivet *et al.* 2011). A central question in the interpretation of the changes detected is that of the depth of the velocity variations. A recent discussion of possible causes for velocity perturbations and their depth range can be found in Sens-Schönfelder & Wegler (2011). Observations of velocity changes that occur at different depths have come from investigations using combinations of borehole and surface sensors, which have allowed the identification of changes at shallow depths (Sawazaki *et al.* 2009; Nakata *et al.* 2011). With interpretations of coda wave measurements, Rivet *et al.* (2011) located changes that occurred at great depth in a subduction zone. Their interpretation was based on the assumption that coda waves

are dominated by Rayleigh waves that follow a two-dimensional (2-D) diffusion process at the free surface. The depth sensitivity is, therefore, limited to the depth sensitivity of the surface waves. In contrast, Sens-Schönfelder & Wegler (2006) investigated shallow velocity changes at a volcano, which they interpreted as a response to changes in the hydrological system. Supported by the lapse-time dependence of the apparent relative velocity change, their interpretation was based on the assumption that the coda is dominated by body waves that show slower decay of the sensitivity with depth.

We know that regions that show tectonic and/or volcanic activity are highly heterogeneous (Aki & Chouet 1975; Aki & Ferrazzini 2000; Abubakirov & Gusev 1990; Sato *et al.* 2012). In particular, heterogeneities located right beneath the free surface convert surface waves into bulk waves, and reciprocally, bulk waves into surface waves (e.g. Larose *et al.* 2005a). In this study, we deal with waves that propagate in media containing vertical and horizontal heterogeneities. We investigate the following questions:

(i) Is the assumption of the surface wave diffusion process sufficient to describe the sensitivity of coda waves, or does the bulk wave diffusion play a role in fully heterogeneous media?
(ii) Can changes at depth be detected if the sources and sensors are placed at the free surface?
(iii) If changes can be detected, what is the depth sensitivity of the coda waves in this multiple scattering regime?
(iv) How can we differentiate between shallow and deep velocity variations?

In this study, we will answer these questions on the basis of 2-D numerical simulations. In Section 2, we describe the elastic heterogeneous medium, introduce the velocity perturbation and characterize the degree of heterogeneity. In Section 3, we separately describe the depth sensitivity kernel of Rayleigh and bulk waves, and propose a linear combination of bulk and surface wave sensitivity to model the depth sensitivity of coda waves. In Section 4, we compare theoretical predictions with numerical simulations. We demonstrate the accuracy of the model for weak changes located at different depths. These theoretical predictions are also tested at different times in the coda and for different degrees of heterogeneity. We emphasize the importance of bulk waves for the depth sensitivity of coda waves collected by arrays at the free surface. We obtain a model that shows the partition ratio of surface wave and bulk wave sensitivity at different times in the coda and for different levels of heterogeneities. In the last part, we use lunar data to demonstrate the practical relevance of our findings.

2 NUMERICAL SIMULATIONS

To study the sensitivity of coda waves to velocity perturbations at depth, we perform numerical simulations of seismic waves in a heterogeneous 2-D elastic medium without intrinsic attenuation. The scattering is weakly anisotropic but the medium itself does not show any preferential direction.

To create the heterogeneous 2-D elastic medium, we follow the procedure described by Frankel & Clayton (1986). The 2-D velocity field has a constant background *P*-wave velocity v_p^0 with superimposed spatial velocity fluctuations $\delta v_p(x, z)$ that constitute the scatterers. The total *P*-wave velocity can be decomposed as

$$v_p(x,z) = v_p^0 + \delta v_p(x,z). \tag{1}$$

The total *S*-wave velocity relates to the total *P*-wave velocity, as $v_s = \frac{v_p}{\sqrt{3}}$, and thus undergoes the same respective velocity variations. The velocity fluctuations $\delta v_p(x, z)$ are themselves characterized by a spatial autocorrelation function. The main statistical parameters that characterize the medium are described in Section 2.1. Fig. 1(A) shows a typical realization of a random medium.

In this initial velocity model, we introduce a small velocity perturbation $\frac{dv}{v}$ in a layer of thickness h at depth d, as shown in Fig. 1(B). The perturbed velocity v_p' in the layer is proportional to the velocity v_p

$$v_p'(x,z) = \begin{cases} v_p(x,z)\cdot(1+\frac{dv}{v}) & \text{for} \quad d < z < d+h, \\ v_p(x,z) & \text{for} \quad z < d \text{ or } z > d+h. \end{cases} \tag{2}$$

We take $v_p^0 = 6500$ m s^{-1} and $dv = 100$ m s^{-1} which corresponds to a relative velocity change of $\frac{dv}{v} = 1.54$ per cent throughout the study.

We simulate a semi-infinite medium with a free surface by imposing three absorbing conditions at the sides and one traction-free condition at the surface. To solve the wave equation, we use the 2-D spectral-element method developed by Komatitsch & Vilotte (1998) and implemented in the SPECFEM2D solver, version 6.1, by Tromp & Komatitsch (2008). An element of the discretization grid is shown within the black lines in Fig. 1(C). We place a receiver array and a source at the free surface.

For the simulations, we use a vertical force as the source mechanism, with a central frequency of $f_0 = 20$ Hz, and a frequency bandwidth of $\Delta f = 12$ Hz. The corresponding wavelength for the *P* wave is $\lambda_0 = \frac{v_p^0}{f_0} = 325$ m. We want to note here that the perturbed layer has a thickness of only 200 m, and it is, therefore, thinner than λ_0. The grid size is 16.8×16.8 km^2 ($50\lambda_0 \times 50\lambda_0$), with a 20 m spatial pitch ($\approx\lambda_0/20$). We compute the displacement $\varphi(t)$ for waves propagating in the initial medium $v_p(x, z)$, and $\varphi\prime(t)$ for waves propagating in the slightly perturbed medium $v_p'(x, z)$. This procedure is reproduced for different depth positions d of the layer. All the important parameters for the simulation are summarized in Table 1. In the following sections, if not stated differently, we only display results for source–receiver distances of 4 km.

2.1 Characterization of the heterogeneous medium

In this part, we characterize the level of heterogeneity of the medium. In Section 2.1.1, we discuss the correlation function that we chose for the random medium in more detail. In Section 2.1.2, we determine the equipartition ratio and therewith the energy velocity ratio. Then in Section 2.1.3, we provide special focus on the determination of the scattering (ℓ) and transport ($\ell^\star$) mean free paths. These quantities are important for the theoretical model in Section 4.

2.1.1 Autocorrelation function of the random medium

For the velocity model $v_p(x, z)$, we decided to work with a von-Karman type autocorrelation function, as this model is consistent with the general observations concerning rock and surface geology, which show very rough behaviours at small length scales (Frankel & Clayton 1986; Holliger & Levander 1992). This correlation function is defined as (Tatarski 1961)

$$N(r) = \frac{1}{2^{m-1}\Gamma(m)}\left(\frac{r}{a}\right)^m K_m\left(\frac{r}{a}\right)\sigma^2, \tag{3}$$

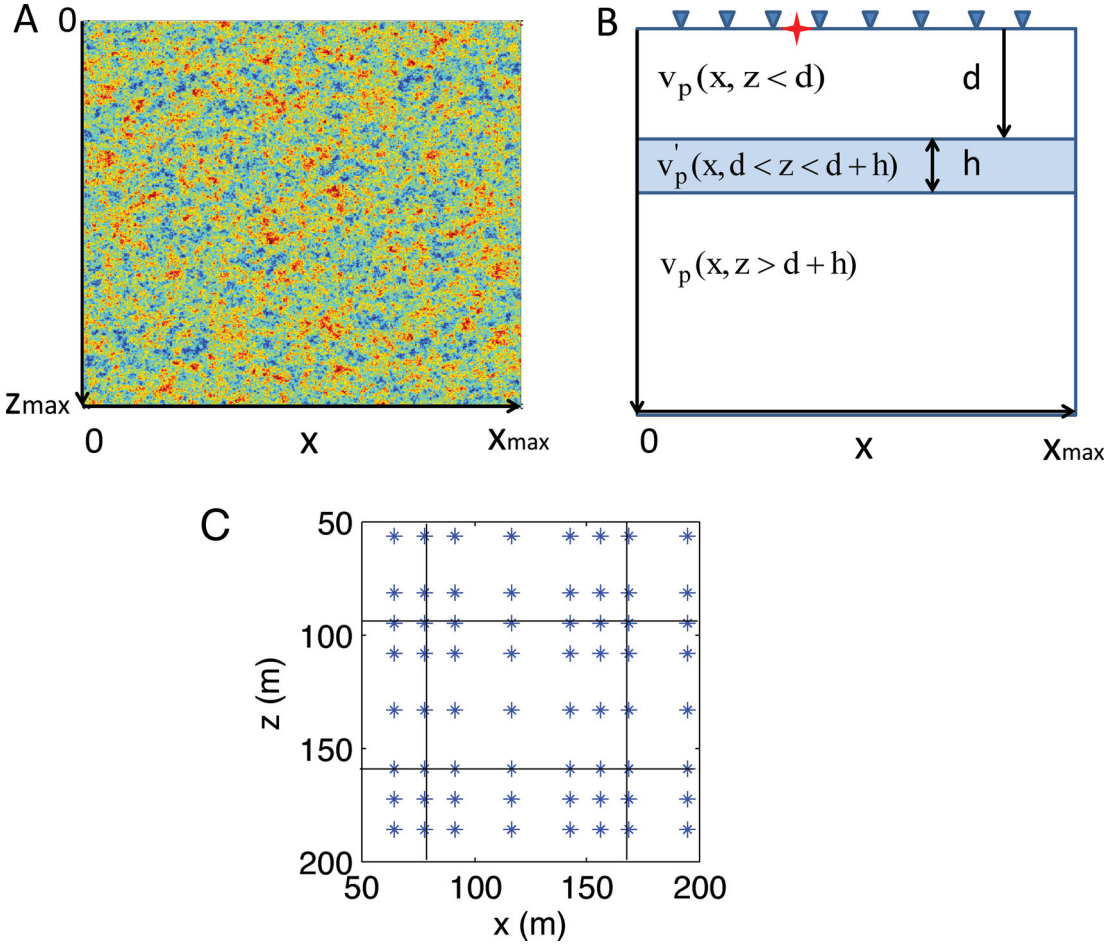

Figure 1. (A) Medium with von-Karman correlation function. The correlation distance is $a \approx \lambda_0$. x and z are $50\lambda_0 \times 50\lambda_0$. (B) Configuration for the study of depth sensitivity. A medium of dimension x, z contains a thin layer (h) with a small velocity perturbation at depth d (note that the thickness of h is exaggerated for better visualization). (C) Grid element used for the simulations. The black lines limit the gridpoints (blue stars) of one element.

Table 1. Physical parameters of the numerical simulations used in this study.

Notation	Value	Description
L	16.8×16.8 km^2	Grid size
Δx, Δz	20 m	Grid spacing
	9 s	Record length
Δt	$3 \cdot 10^{-4}$s	Time step
f_0	20 Hz	Source frequency
Δf	12 Hz	Source bandwidth
a	300 m	Correlation length
σ	5, 10, 15, 20, 30 per cent	Velocity fluctuations
v_p		Initial P-wave velocity field
v_p'		Perturbed P-wave velocity field
v_p^0	6500 m s^{-1}	Mean P-wave velocity
v_s^0	3750 m s^{-1}	Mean S-wave velocity
λ_0	325 m	Central P-wavelength
h	200 m	Thickness of perturbed layer
d		Depth of perturbed layer
$\frac{dv}{v}$	1.54 per cent	Relative velocity change
ε		Apparent relative velocity change

where $K_m(x)$ is a modified Bessel function of order m, $\Gamma(m)$ is the gamma function, r is the offset (or spatial lag), a is the correlation distance and σ the relative standard deviation of the velocity. We consider a specific type of von Karman function, where m is 0.5. For this case, the 2-D Fourier transform $\Phi_{\text{Karman}}(k_r)$ that represents the power spectrum of the medium fluctuations, is given by

$$\Phi_{\text{Karman}}(k_r) = \frac{a^2}{1 + k_r^2 a^2}\sigma^2, \tag{4}$$

where k_r is the radial wavenumber. We chose $a \approx \lambda_0$ to allow strong interactions between waves and heterogeneities, and to enhance scattering. σ ranges from $\sigma = 5$–30 per cent. For each configuration, we perform numerical simulations in ten different media that obey the same statistics (for averaging purposes).

2.1.2 Equipartition ratio

In a heterogeneous elastic medium, waves propagate both as P and S waves, and they are repeatedly converted from one state to another. The available elastic energy in the phase space at long times will be equally distributed among all of the possible states of the P and S waves (Weaver 1982, 1985). This phenomenon is referred to as the equipartition of seismic waves (Hennino *et al.* 2001). In an unbounded 2-D medium, the modes are plane waves with either SV or P polarization. If $v_s = \frac{v_p}{\sqrt{3}}$, the equipartition ratio in 2-D reads

$$\langle S^2 \rangle / \langle P^2 \rangle = 3, \tag{5}$$

where S and P are the amplitudes of the S and P waves, respectively. To verify the equipartition ratio, we place a source close to the free surface. We then place 150 receivers in a vertical line in

the middle of the medium. The top receiver is still several wavelengths away from the free surface. We calculate the energy ratio between the squared curl and the squared divergence of the wavefield in a gliding time-section. We average over the time sections and 50 realizations of the random medium. The data yield a ratio of $\langle S^2\rangle/\langle P^2\rangle = 3.4$. Repeating the experiment and considering four reflecting boundaries yields a ratio of exactly 3. We conclude that the difference between the experiment with a free surface and three absorbing boundaries and the theory for infinite space is due to the absorbing boundary conditions and the surface. Boundaries appear to absorb *P* waves more quickly than *S* waves. The energy velocity c which reflects the celerity at which the seismic energy is transported, can thus be approximated according to the energy ratio

$$\frac{1}{c} = \frac{0.77}{v_s} + \frac{0.23}{v_p}. \tag{6}$$

2.1.3 *Determination of the scattering mean free path*

In a regime where multiple scattering is very strong, waves travelling from a source to a receiver follow many trajectories. In this case, wave propagation can be considered as a random walk process, and can be described to a good approximation by the diffusion equation (for further information, see for example the review of Margerin & Nolet 2003). Within this approximation, the multiply scattered waves that propagate in n dimensions are described by the energy velocity c, the transport mean free path $\ell^\star$ or the diffusion coefficient as

$$D = \frac{c\ell^\star}{n}. \tag{7}$$

We need the scattering mean free path ℓ and the transport mean free path $\ell^\star$ for the modelling of the depth sensitivity of coda waves. ℓ is a central quantity in radiative transfer and diffusion theory. It represents the typical length scale after which a beam with a given propagation direction has been significantly attenuated by scattering. $\ell^\star$ is the distance after which the 'memory' of the initial direction of the beam is lost (Sato 1993; Paasschens 1997). $\ell^\star$ is related to the scattering mean free path via

$$\ell^\star = \frac{\ell}{1 - \langle\cos\theta\rangle}, \tag{8}$$

where $\langle\cos\theta\rangle$ is the directional average of the cosine of the scattering angle. When the scattering is isotropic (i.e. inhomogeneities scatter equal amounts of energy in all directions), $\ell^\star = \ell$. In our case, where the correlation length and wavelength are similar ($a \approx \lambda_0$), scattering is not completely isotropic. We would expect $\ell^\star > \ell$ according to eq. (8).

In the following, we determine $\ell^\star$ and ℓ numerically from the coherent and incoherent parts of the recorded signals. The coherent part of the waveform is the wave that resists averaging over different realizations of disorder. The incoherent part of the waveform is constituted by waves vanishing while averaging over disorder.

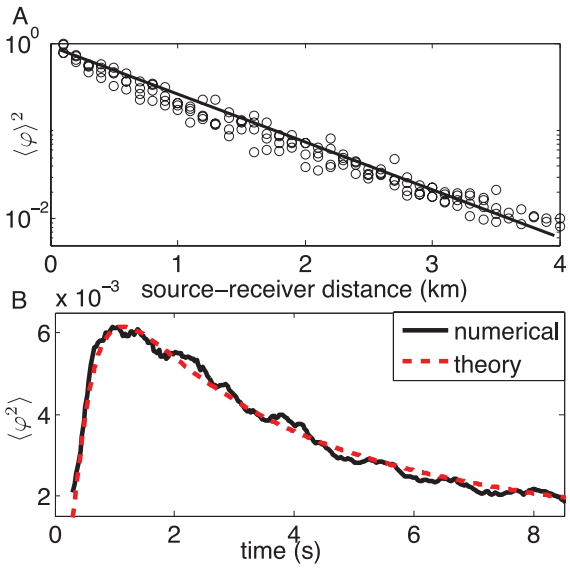

Figure 2. (A) Logarithm of the normalized coherent intensity $\langle\varphi\rangle^2$ versus source–receiver distance averaged over 50 simulations. After correcting the geometrical spreading, the slope is proportional to $-1/\ell$. (B) Normalized incoherent intensity $\langle\varphi^2\rangle$ versus time. $\ell^\star$ is calculated from the diffusion constant of the diffusion equation that gives the best fit.

We arrange 148 receivers in a cross-shape array in the initial heterogeneous medium. The spacing between the receivers is 200 m. The source is placed in the centre of the receivers. For this simulation, all four of the boundaries are reflecting. To have enough data to average, we ran 50 realizations with this configuration in media that obey the same statistics.

From the coherent part $\langle\varphi(t)\rangle$ of the waveform, we determine the scattering mean free path ℓ following Derode *et al.* (2001). The power spectrum of the coherent signal $|\langle H(\omega)\rangle|^2$ is linked to the scattering mean free path ℓ via

$$|\langle H(\omega)\rangle|^2 = \exp\left(-\frac{x}{\ell}\right), \tag{9}$$

where x denotes the distance between source and receiver in the medium. In Fig. 2(A), we plot the logarithm of the normalized energy versus the source–receiver distance. The slope of the regression line is $-1/\ell$. The results for different σ are given in Table 2.

From the incoherent part of the waveform, we determine the transport mean free path $\ell^\star$. We look at the energy envelope of the waveforms. We take a sliding time window of $2T = 0.3$ s, which corresponds to six periods, and we calculate the average intensity in this window according to

$$I(t) = \langle\varphi(\tau)^2\rangle_{\tau\in[t-T,t+T]}. \tag{10}$$

We then average the intensity over 50 models that obey the same statistics. We search for the diffusion constant D that gives the best fit with the diffusion Equation and we calculate $\ell^\star$, as in eq. (7). In

Table 2. Scattering mean free path and transport mean free path calculated experimentally for models with different amounts of heterogeneity.

Model	Scattering mean free path (ℓ)	Transport mean free path ($\ell^\star$)
$\sigma = 5$ per cent	10 000 m ±10 per cent	13 000 m ±15 per cent
$\sigma = 10$ per cent	2200 m ±7 per cent	2700 m ±15 per cent
$\sigma = 15$ per cent	1200 m ±5 per cent	1500 m ±10 per cent
$\sigma = 20$ per cent	900 m ±5 per cent	940 m ±5 per cent
$\sigma = 30$ per cent	500 m ±2 per cent	450 m ±3 per cent

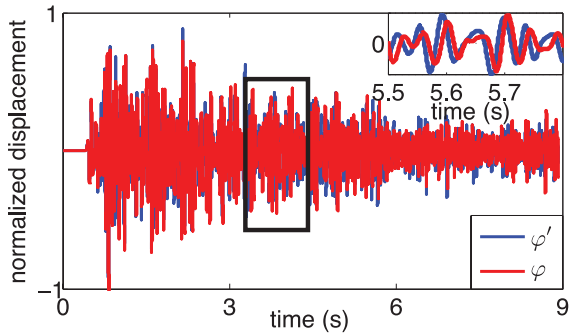

Figure 3. Synthetic seismograms recorded with (blue) and without (red) perturbed layer at 50 m in depth. The black box indicates the a time window for the stretching around 3.6 s. Inset: zoom in on the unperturbed and perturbed seismograms.

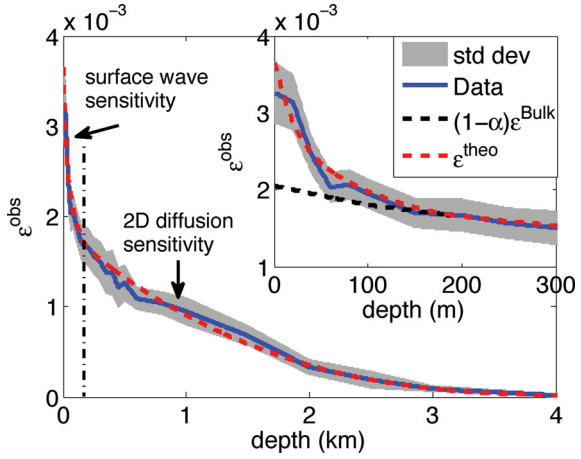

Figure 4. Apparent relative velocity changes with depth of the perturbed layer averaged over ten realizations ($\sigma = 20$ per cent). We can discriminate two different regimes of sensitivity for a shallow and a deep perturbed layer marked by the black chain line. The modelled data (dashed-red) $\varepsilon^{\text{theo}}(d, t =$ 3.6s) for the depth sensitivity of coda waves fit the observations very well. Inset: importance of the surface waves to describe the depth sensitivity, as the bulk regime $(1 - \alpha)\varepsilon^{\text{Bulk}}$ alone cannot account for the steep slope at short times.

Fig. 2(B) we illustrate the intensity for a model with $\sigma = 20$ per cent and its fit with the diffusion equation.

Table 2 gives the results for the scattering mean free paths that were obtained from numerical calculations for media with different degrees of heterogeneity σ. We note that ℓ and $\ell^\star$ have close values, which indicates only weakly anisotropic scattering ($\ell \approx \ell^\star$). The uncertainties for the measures are the standard deviations that we obtained by averaging over 50 models.

2.2 Determination of the apparent relative velocity changes with the stretching technique

We now use the numerical simulation with one free surface and three absorbing boundaries. We run a first experiment with an initial model v_p, and then a second with a perturbed velocity v_p' in a layer. Fig. 3 shows the seismograms for an initial (blue) and a perturbed (red) medium for a receiver 2 km away from the source. The disturbance occurs at 50 m in depth in a medium with velocity fluctuations of $\sigma = 20$ per cent. By zooming into the coda of the seismograms, we can see that the perturbed seismogram lags behind in time with respect to the unperturbed seismogram, while the shape of the wave train remains largely unchanged.

We use the stretching technique to analyse these apparent relative velocity changes in the coda of the perturbed seismograms (Lobkis & Weaver 2003; Sens-Schönfelder & Wegler 2006). We assume that the perturbation of the signal can be measured as the effect of a slight change of its global velocity $\delta V/V$. It has been stretched or compressed in time in comparison to the unperturbed signal by a factor $t(1 - \varepsilon)$, where $\varepsilon = \delta V/V$. To obtain the optimal value for $\delta V/V$, we test systematically various values of ε. For each ε we calculate the correlation coefficient CC of the perturbed stretched signal $\varphi\prime$ and the unperturbed signal φ

$$CC(\varepsilon) = \frac{\int_{t_1}^{t_2} \varphi'\,[t(1-\varepsilon)]\,\varphi\,[t]\,\mathrm{d}t}{\sqrt{\int_{t_1}^{t_2} \varphi'^2\,[t(1-\varepsilon)]\,\mathrm{d}t \int_{t_1}^{t_2} \varphi^2\,[t]\,\mathrm{d}t}}, \tag{11}$$

where t_1 and t_2 are the beginning and end of the time window used. The value of ε, that maximizes the cross-correlation coefficient between the perturbed and the unperturbed signals at a given time corresponds to the observed value ε^{obs} of the apparent relative velocity change. For more detailed information, the reader should refer to Hadziioannou *et al.* (2009), for example. We apply this procedure to calculate the apparent relative velocity changes for all of the depth positions of the perturbed layer. The length of the time window is 1.5 s, and it is centred at different times in the coda.

2.3 Results for the apparent relative velocity changes with depth

When analysing the apparent relative velocity changes ε^{obs} versus the depth of the perturbed layer in Fig. 4, we observe a decrease of ε^{obs} with depth, which testifies to reduced sensitivity of our measurements to changes at greater depths. We can discriminate two different regimes of sensitivity: for shallow and deep perturbed layers. Their separation is marked in Fig. 4 with the dash-dotted black line. In the first regime, which concerns the early part of the slope, the sensitivity of ε^{obs} decays rapidly with depth, until a depth of approximately half the central wavelength λ_0. In the second regime, which concerns the later part of the slope, the slower decay results in a deeper sensitivity.

We interpret the rapid decay (shallow perturbed layers) as the footprint of the vertical depth sensitivity of the fundamental mode of the surface waves. For perturbations at greater depths (deep perturbed layers), we propose a model based on 2-D diffusion of body waves. We will show in the following sections that we can model the apparent relative velocity changes $\varepsilon^{\text{Bulk}}$ and $\varepsilon^{\text{Surf}}$, computed for the bulk and surface wave sensitivities according to

$$\varepsilon^{\text{theo}}(d, t) = \alpha(t)\varepsilon^{\text{Surf}}(d) + (1 - \alpha(t))\varepsilon^{\text{Bulk}}(d, t), \tag{12}$$

where $\varepsilon^{\text{theo}}(d, t)$ is the modelled relative velocity change and α the fitting parameter, or the partition coefficient. Note that this partition coefficient is different from the equipartition ratio, as it integrates the time spent in each state of the wave (bulk or surface). In Section 3, we study the computation of the relative velocity changes $\varepsilon^{\text{Bulk}}$ and $\varepsilon^{\text{Surf}}$ in the bulk and surface wave sensitivity regime independently.

3 MODELLING THE TWO SENSITIVITY KERNELS

In this section, we describe the 1-D surface wave regime and the 2-D diffusion regime, which we use to model the depth sensitivity of the coda waves. For the bulk waves, we will compare an approach based on the diffusion solution to an approach based on the radiative transfer solution.

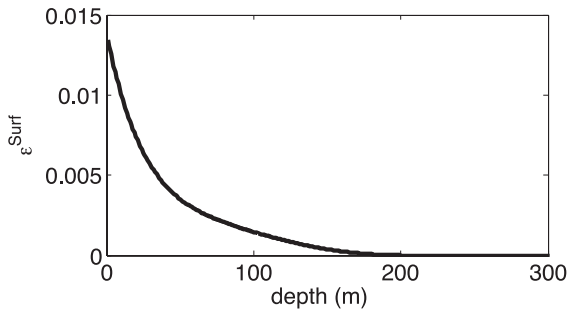

Figure 5. Apparent relative velocity changes $\varepsilon^{\mathrm{Surf}}(d)$ for the 1-D surface wave sensitivity regime as a function of the depth of the perturbed layer.

3.1 Surface wave sensitivity

To study the depth penetration of surface wave energy independent of bulk waves, we propagate a pulse in a homogeneous medium (constant velocity, no fluctuations). This medium does not allow conversion scattering into bulk waves. Similar to the previous numerical simulations, we introduce a thin layer with a slightly different velocity ($\frac{dv}{v} = 1.54$ per cent). Fig. 5 shows the apparent relative velocity changes $\varepsilon^{\mathrm{Surf}}(d)$ versus the depth of the layers that were measured from the direct arrivals. As can be seen, the surface wave sensitivity decays very rapidly with depth and disappears entirely after 2/3 of the central wavelength λ_0.

3.2 Bulk sensitivity: the diffusive kernel approach

As we have seen previously, the apparent relative velocity changes of the seismograms can be quantified by a stretching factor $\varepsilon^{\mathrm{obs}}$. The theoretical bulk contribution $\varepsilon^{\mathrm{Bulk}}$ can be related to a local velocity perturbation using the sensitivity kernel introduced by Pacheco & Snieder (2005)

$$K(\boldsymbol{S}, \boldsymbol{R}, \boldsymbol{r}_0, t) = \frac{\int_0^t p(\boldsymbol{S}, \boldsymbol{r}_0, u) p(\boldsymbol{r}_0, \boldsymbol{R}, t-u) du}{p(\boldsymbol{S}, \boldsymbol{R}, t)}, \tag{13}$$

where $\boldsymbol{S}$ and $\boldsymbol{R}$ are the positions of the source and the receiver, $\boldsymbol{r}_0$ is the position of the local velocity variation and t is the centre of the time interval in the coda where the stretching is evaluated. Here, $p(\boldsymbol{a}, \boldsymbol{b}, t)$ is the probability that the wave has travelled from $\boldsymbol{a}$ to $\boldsymbol{b}$ during time t. This can be approximated by the intensity of the wavefield from $\boldsymbol{a}$ to $\boldsymbol{b}$ at time t. An example of the sensitivity kernel is shown in Fig. 6 at $t = 3.6$ s in the coda for a source and receiver inside the medium. This sensitivity kernel is relevant in the multiple scattering regime, and it can be interpreted as the volumetric density of time that the scattered waves spend at $\boldsymbol{r}_0$. It can be noted that the total time t spent in the medium is retrieved by integrating the kernel over the volume of the studied medium

$$\begin{aligned} t &= \int_{\mathrm{medium}} K(\boldsymbol{S}, \boldsymbol{R}, \boldsymbol{r}, t) \mathrm{d}\boldsymbol{r} \\ &= \int_{x=0}^{x_{\max}} \int_{z=0}^{z_{\max}} K(\boldsymbol{S}, \boldsymbol{R}, x, z, t) \mathrm{d}x \mathrm{d}z, \end{aligned} \tag{14}$$

where $\boldsymbol{r} = x\boldsymbol{e}_x + z\boldsymbol{e}_z$. $(\boldsymbol{e}_x, \boldsymbol{e}_z)$ are cartesian unit vectors. This kernel can also relate the scattering cross-section of a defect appearing in a multiple scattering medium to a correlation coefficient extracted from the coda (Larose *et al.* 2010; Rossetto *et al.* 2011).

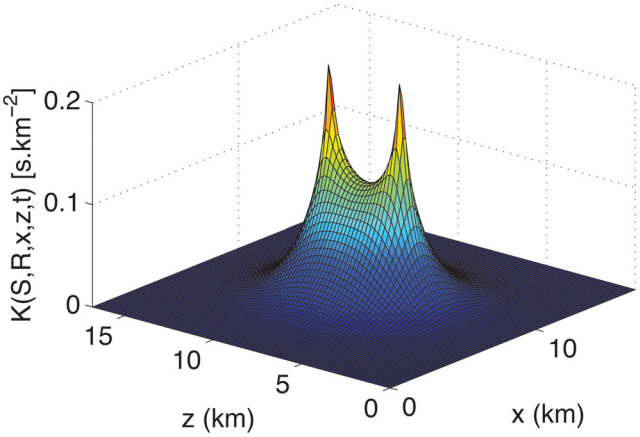

Figure 6. Spatial representation of sensitivity kernel *K(S,R,x,z,t)* in the diffusion approximation at $t = 3.6$ s. The two peaks correspond to the positions of the source and receiver.

For a local velocity variation $\frac{dv}{v}$ in an elementary volume ΔV centred on $\boldsymbol{r}_0$, the stretching coefficient $\varepsilon^{\mathrm{Bulk}}(\boldsymbol{r}_0, t)$ for signals emitted in $\boldsymbol{S}$ and received in $\boldsymbol{R}$ reads

$$\varepsilon^{\mathrm{Bulk}}(\boldsymbol{r}_0, t) = \frac{K(\boldsymbol{S}, \boldsymbol{R}, \boldsymbol{r}_0, t)}{t} \frac{dv}{v} \Delta V. \tag{15}$$

In our numerical experiment, the velocity variation is applied to a layer of thickness h located at a depth d. As the velocity variation is weak, the measured stretching coefficient can be expressed as the spatial integral of the kernel on the medium, weighted by the applied velocity change

$$\begin{aligned} \varepsilon^{\mathrm{Bulk}}(d, t) &= \int_{\mathrm{medium}} \frac{K(\boldsymbol{S}, \boldsymbol{R}, \boldsymbol{r}, t)}{t} \frac{dv}{v}(\boldsymbol{r}) \mathrm{d}\boldsymbol{r} \\ &= \int_{x=0}^{x_{\max}} \int_{z=d}^{z=d+h} \frac{K(\boldsymbol{S}, \boldsymbol{R}, x, z, t)}{t} \frac{dv}{v} \mathrm{d}x \mathrm{d}z, \end{aligned} \tag{16}$$

with the velocity change $\frac{dv}{v}(\boldsymbol{r}) = \frac{dv}{v}$ in the layer and $\frac{dv}{v}(\boldsymbol{r}) = 0$ elsewhere.

3.2.1 *Intensity propagator in the diffusion approximation*

As a first approximation, we describe the intensity propagator in eq. (13) with the diffusion equation solution

$$p(\boldsymbol{S}, \boldsymbol{R}, t) = \frac{1}{4\pi Dt} e^{\frac{-\|\boldsymbol{S}-\boldsymbol{R}\|^2}{4Dt}} \tag{17}$$

where D is the diffusion constant that depends on the medium heterogeneity. Eq. (17) stands for 2-D infinite media. To take the free surface into account, a semi-infinite space has to be considered. In this case, the solution is found in terms of the sum of the infinite medium solution and its mirror image from the free surface. This solution can be easily computed and gives an analytical solution of the kernel (eq. 13). Nevertheless, this kernel is only accurate when the diffusion approximation is valid: at times much greater than the transport mean free time $t \gg t^\star$, where $t^\star = \ell^\star/c$, and for velocity variations located far away from the sensors.

3.2.2 *Intensity propagator for a radiative transfer approximation*

The radiative transfer equation allows for a more general representation of wave intensities in scattering media. In our case of weakly

anisotropic scattering ($\ell^\star \approx \ell$), we assume that we can use the following exact solution (Sato 1993; Paasschens 1997), valid for 2-D isotropic scattering:

$$p(r,t) = \frac{e^{-ct/\ell}}{2\pi r}\delta(ct-r) + \frac{1}{2\pi\ell ct}\left(1-\frac{r^2}{c^2t^2}\right)^{-\frac{1}{2}} e^{[\ell^{-1}(\sqrt{c^2t^2-r^2}-ct]}\Theta(ct-r), \quad (18)$$

where c is the energy velocity, r is the distance between source and receiver, ℓ is the scattering mean free path and $\Theta(x)$ is the Heaviside (or step) function. The first term describes the coherent part of the intensity that decreases exponentially with the distance relative to the scattering mean free path. The second term describes the diffuse intensity. We note that the diffusion solution is reached when $t \gg r/c$.

3.2.3 *Bulk sensitivity kernel in an infinite medium*

As the next step, we want to see how well the diffusion or radiative transfer approach models the bulk sensitivity of our data. For this purpose, we study the bulk waves without influence of the surface waves. Therefore, we slightly change the configuration of our numerical simulations. We place the source and the horizontal receiver array within the medium at a depth of 8.8 km, and take absorbing conditions at all four boundaries. With this configuration, we would not expect any surface waves to appear on our record, and so the apparent relative velocity changes should only be governed by the 2-D propagation of bulk waves.

The resulting apparent relative velocity changes $\varepsilon^{\rm obs}(d, t = 3.6{\rm s})$ are shown in blue in Fig. 7, versus the depth of the perturbed layer for a heterogeneity of $\sigma = 20$ per cent. The error bars indicate the standard deviation over 10 models. We also plot $\varepsilon^{\rm Bulk}$ from the diffusion-based kernel in black and from the radiative-transfer-based kernel in red (Fig. 7). As expected, the main difference between the diffusion and radiative transfer approach is visible for small offsets to the source; i.e., when the time until visiting the layer is small. For long distances, the difference between the two approaches is negligible: both of the approaches fit the data very well at large distances from the source. For distances smaller than one scattering mean free path, the diffusion equation is not valid yet, and it underestimates the expected apparent relative velocity changes. This problem is solved by the radiative transfer approach, which is accurate at short times. We will, therefore, take the radiative transfer approach to model the depth sensitivity. We emphasize that $\varepsilon^{\rm Bulk}$ from the radiative-transfer in Fig. 7 directly fits the data (no free parameters). The small discrepancies between the observation and model might be a result of the effective diffusivity that we used in the model, as we cannot measure the scattering mean free path for *P* and *S* waves separately (Turner 1998).

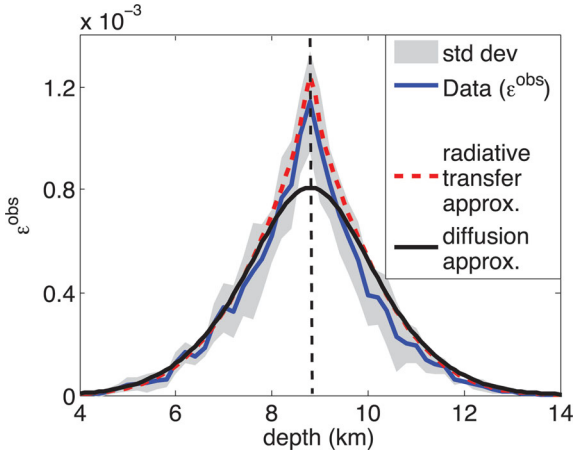

Figure 7. Apparent relative velocity changes $\varepsilon^{\rm obs}(d, t = 3.6{\rm s})$ versus depth of the perturbed layer for bulk waves in an infinite medium with $\sigma = 20$ per cent. The black line shows $\varepsilon^{\rm bulk}$ in the diffusion approximation and the dashed-red line $\varepsilon^{\rm bulk}$ in the radiative transfer approximation. The vertical broken black line marks the positions of the source and the receivers.

4 MODEL FOR THE DEPTH SENSITIVITY

To obtain a theoretical model $\varepsilon^{\rm theo}(d, t)$ that describes the coda-wave sensitivity at depths, according to eq. (12), we now combine the surface wave part and the bulk part. For the bulk regime, we apply the radiative transfer approach. Fig. 4 shows the depth sensitivity averaged over 10 models with $\sigma = 20$ per cent velocity fluctuations. The source and receivers are placed at the free surface. The time window in the coda was centred around 3.6 s. With the minimum mean-square error criterion, we search the partition coefficients α for the surface waves and $1 - \alpha$ for the bulk waves, that optimize the fit of the depth sensitivity from the numerical simulations. In this case, the best fit to the experimental slope is obtained with a partition ratio of 1/4 for surface to bulk waves ($\alpha = 0.25$). The ratio between the coefficients implies that the waves spent more time as bulk waves than as surface waves. As we can see in Fig. 4, the proposed model gives an excellent fit. The zoom at small distances indicates the need to consider surface waves in the model. In black, we see the fit using the sensitivity of bulk waves only (Fig. 4). The steep slope over short distances is due to the rapidly vanishing sensitivity of the surface waves versus the depth.

According to eq. (15), which is written for weak velocity changes, the observed apparent relative velocity changes $\varepsilon^{\rm obs}$ depend linearly on the velocity changes $\frac{dv}{v}$ introduced in the perturbed layer. This is shown in Fig. 8, where the apparent relative velocity changes at a receiver at close distance to the source are computed. The perturbed layer is at 500 m in depth, and its velocity is successively increased by 1, 2, 4 and 8 per cent.

In the following, we now look at the behaviour of the depth sensitivity and the evolution of the partition coefficient α by considering:

(i) different levels of heterogeneity (σ) in the model, in Section 4.1.

(ii) different time windows in the coda, in Section 4.2.

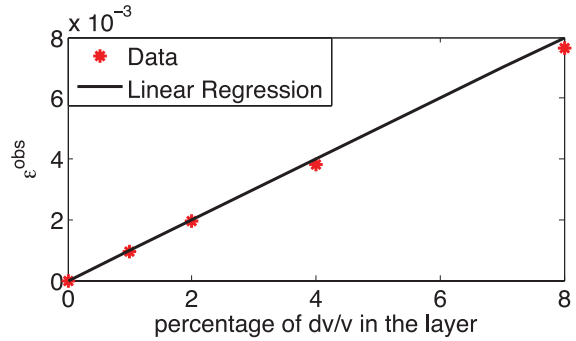

Figure 8. Apparent relative velocity changes $\varepsilon^{\rm obs}(d, t = 3.6{\rm s})$ versus the degree of perturbation in the layer. The layer is at 500 m in depth, and the receiver in the immediate vicinity of the source.

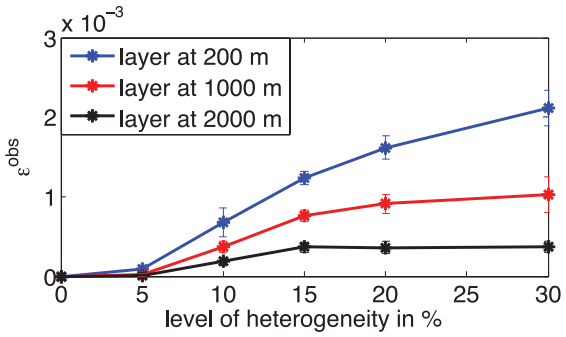

Figure 9. Depth sensitivity $\varepsilon^{\mathrm{obs}}(d, t = 3.6\mathrm{s})$ computed for different levels of heterogeneity towards changes occurring at 200, 1000 and 2000 m in depth.

4.1 Different degrees of heterogeneity

In this section, we report on the results of the simulations with different levels of heterogeneity. To that end, we repeat the same types of simulations as described in Section 2, using a free surface and three absorbing boundary conditions. We use velocity fluctuations of $\sigma = 5$, 10, 15, 20 and 30 per cent for the random elastic medium. In Fig. 9, we look at the apparent relative velocity changes $\varepsilon^{\mathrm{obs}}(d, t = 3.6\mathrm{s})$ averaged over ten models versus the degree of heterogeneity for three depth positions of the layer (200, 1000, 2000 m). We see clearly that waves travelling in media with little heterogeneity ($\sigma = 5$ per cent) are hardly sensitive to perturbations at depth, even to perturbations at 200 m depth only. The medium is not heterogeneous enough to cause significant conversion from Rayleigh to bulk waves, and vice versa. Therefore, the depth sensitivity is dominated by surface waves and limited to their penetration depth. When the medium becomes more heterogeneous ($\geq$10 per cent), the bulk waves start to have an important role, and the coda waves become sensitive to changes at greater depths. This is even more emphasized in very heterogeneous medium (20–30 per cent), where an important apparent relative velocity change $\varepsilon^{\mathrm{obs}}$ is obtained for changes at greater depth. Such heterogeneous regimes are dominated by bulk waves.

This behaviour can also be seen in Fig. 10, where we report on the evolution of the partition coefficient α for surface waves and $1 - \alpha$ for bulk waves with time in the coda, for models with degrees of heterogeneity ranging from 5 to 30 per cent. At the moment, we focus only on values at 3.6 s, marked by black vertical lines in Fig. 10, and discuss the time dependence in Section 4.2. Consistent with the previous observations, in media with heterogeneities of only 5 per cent, the partition coefficient for surface waves is at $\alpha = 0.97$. In media with heterogeneities of 10 per cent, $\alpha = 0.8$. In media with $\sigma = 15$ per cent, we observe that $\alpha = 0.32$. For strongly heterogeneous media, bulk waves clearly dominate over surface waves with $\alpha = 0.17$ for $\sigma = 20$ per cent and $\alpha = 0.1$ for $\sigma = 30$ per cent.

At this lapse time ($t = 3.6$ s), the depth sensitivity is limited to the penetration depth of surface waves for weakly heterogeneous media, whereas in media with an increased amount of heterogeneity body waves play an prominent role.

4.2 Different times in the coda

In this section, we study the depth sensitivity at different times in the coda. To this end, we calculate the apparent relative velocity changes in different time windows in the coda, scanning a range from 1.8 to 6.6 s. Fig. 11 shows the results for a model with velocity variations of $\sigma = 20$ per cent at three different times (1.8, 3.6 and 6.6 s). The importance of surface waves at shallow depths for early times in the coda is seen clearly. At later times in the coda, the bulk waves become increasingly important.

To have a more quantitative approach, we can study the evolution of the partition coefficients with time in the coda, as shown in Fig. 10 for different heterogeneities. For media with heterogeneities of $\sigma =$ 5 per cent, surface waves dominate bulk waves at all times in the coda. For media with heterogeneities of $\sigma = 10$ per cent, there is a crossing of α and $1 - \alpha$ at 5.4 s. Afterwards the sensitivity of the bulk waves is greater than that of the surface waves. Media with heterogeneities of $\sigma = 15$ per cent also show the crossing from

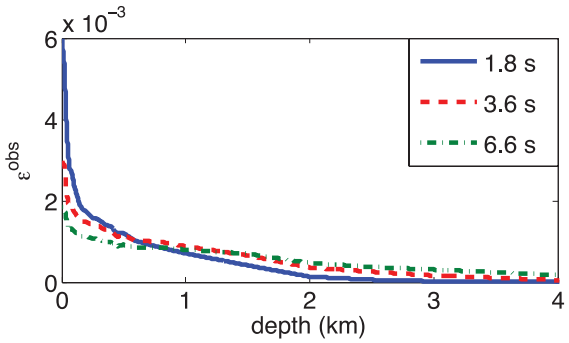

Figure 11. Depth sensitivity computed at different times in the coda for $\sigma = 20$ per cent. Note the importance of the surface wave sensitivity for early times in the coda.

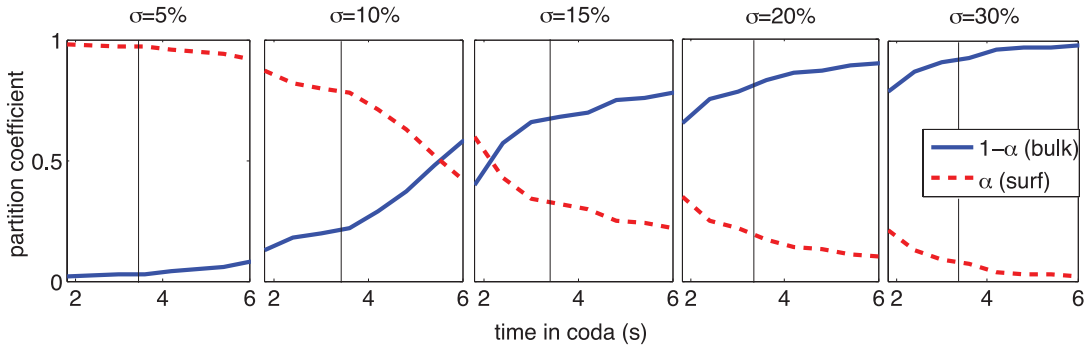

Figure 10. Evolution of the partition coefficients with time in the coda for models with degrees of heterogeneity ranging from 5 to 30 per cent. In dashed red, the partition coefficient α for the surface wave sensitivity, and in blue, $1 - \alpha$ for the bulk wave sensitivity. The black vertical lines mark the processed times at $t = 3.6$ s.

surface wave dominance to bulk wave dominance, although much earlier, at about 2.1 s, which indicates that due to the increased amount of scattering there have been much more surface wave to bulk wave conversions at an early time in the coda. At later times, α appears to stabilize. For strongly heterogeneous media with $\sigma =$ 20 and 30 per cent, bulk waves dominate surface waves at all times in the coda. We observe a continuous slow decrease for α in the case of $\sigma = 20$ per cent and for early times in $\sigma = 30$ per cent. For times after 4 s in the case of $\sigma = 30$ per cent, the bulk wave to surface wave contribution is stabilized with a marginal contribution of surface waves.

Looking at the ensemble of subplots in Fig. 10, the evolution of the partition coefficients for different heterogeneities appears to be complementary. To prove this, we normalize the time axis by the transport mean free time $t^\star = \ell^\star/c$ and plot the partition coefficients against the new, dimensionless axis $t/t^\star$. The result is shown in Fig. 12 for all heterogeneities. The crossing point of the partition coefficients for surface waves and bulk waves coincides quite well for all of the different heterogeneities. The surface waves dominate the depth sensitivity for about six mean free times. For later times, the bulk waves dominate.

A very interesting aspect that emerges from the time dependence in the coda is that we can discriminate a change that occurs at the surface from a change that occurs at depth by looking at the shape of the apparent relative velocity changes ε^{obs} only. Fig. 13 shows ε^{obs} versus the time in the coda: (A) for very shallow positions of the perturbed layer (20 m) and (B) for profound depths (1500 m) of the layer. For perturbations at shallow depth, the surface waves have an important role in the depth sensitivity of the coda waves. Their contribution is high at early times in the coda and decreases at later times. This is what we see as a decay in ε^{obs} on Fig. 13(A). For perturbations at greater depth, the contribution of the surface waves to the depth sensitivity of the coda waves is negligible. Bulk waves have an important role here. At late times in the coda, the time increases that bulk waves have spent on average at greater depth, sampling the area more densely. The depth sensitivity consequently increases with time in the coda. This is why there is an increase in the apparent relative velocity changes ε^{obs} in Fig. 13(B).

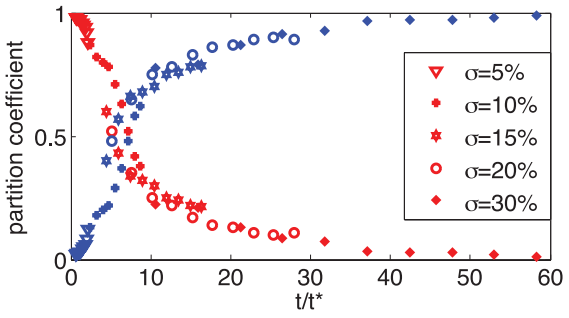

Figure 12. Evolution of the partition coefficients for different degrees of heterogeneity in the medium ranging from 5 to 30 per cent. The time axis has been normalized by the transport mean free time $t^\star = \ell^\star/c$. In red the partition coefficients α for the surface wave sensitivity, and in blue $1 - \alpha$ for the bulk wave sensitivity. The surface waves dominate for the first six mean free times.

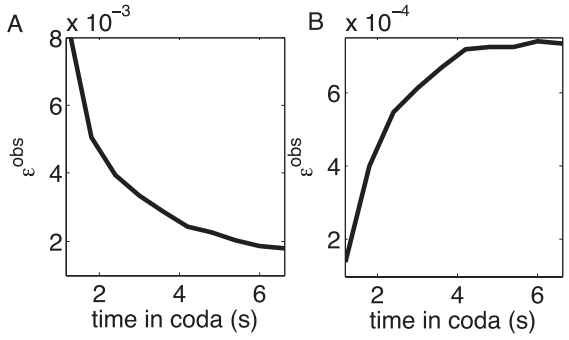

Figure 13. Apparent relative velocity changes ε^{obs} versus time in the coda. Panel (A) for a layer at shallow depth (20 m) and panel (B) for a layer at great depth (1500 m).

4.3 Practical application for shallow depth

To demonstrate the practical relevance of the findings in this study, we re-visit the investigations of Sens-Schönfelder & Larose (2008, 2010), who analysed the data from the Lunar Passive Seismic Experiment of the Apollo 17 mission. Similar to many data sets on Earth the ambient noise recorded during the Apollo era has been analysed with the principles of seismic interferometry to obtain Green's functions between stations by correlation of the ambient noise field. Although the lunar seismic noise has different origin and the subsurface structure differs notably from Earth, the Green's functions exhibit a surface wave part that was used by Larose *et al.* (2005b) to image the subsurface. The coda part of the Green's functions was investigated by Sens-Schönfelder & Larose (2008) to measure the apparent velocity variation in the lunar subsurface over a period of eight day-night cycles on the Moon (about eight months).

The Green's functions obtained from the Apollo data thus have similar properties as their counterparts on Earth and the signals in the numerical simulation in this study. Interestingly the environmental conditions on the Moon affecting the subsurface velocities are much better known than on Earth because of absent tectonics and atmosphere. This renders the data set ideal to illustrate the concepts developed in this paper.

We construct daily cross-correlation functions (CCF) between the six possible sensor pairs by correlating all available 24 h segments of lunar noise. Apparent relative velocity changes were estimated in different time windows of the CCFs with the stretching technique (Section 2.2) in comparison to a reference trace obtained by averaging all daily CCFs for each pair. Velocity variations show a periodicity of one month and were modelled as the consequence of temperature variations induced by the solar irradiation with its day and night cycle.

Thanks to this well-controlled surface process that limits velocity changes to the shallow subsurface we can verify the predictions about the lapse time dependence of the apparent velocity change illustrated in Fig. 13 with real seismic data. Measured in different time windows the apparent velocity curves are merely identical and differ only in their amplitude. Fig. 14 shows the lapse time dependent factor that scales the amplitudes of the apparent relative velocity variations obtained from different lapse times windows. After the passage of the ballistic surface wave train associated with the maximum of the apparent velocity change we observe a decrease with increasing lapse time. This is exactly the predicted behaviour for a near surface velocity perturbation because of the transition from surface wave sensitivity at early times to bulk wave sensitivity at later times as illustrated in Fig. 13.

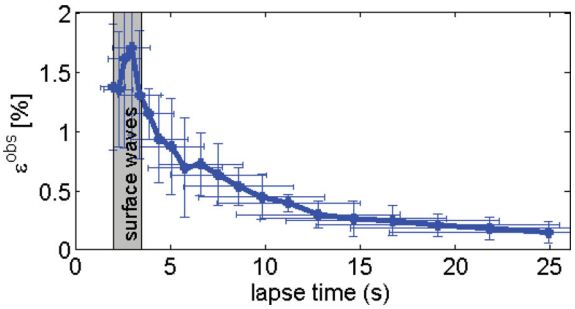

Figure 14. Relative amplitude of the apparent relative velocity changes computed for the lunar data. Velocity changes at the moon are limited to the shallow subsurface and verify the prediction about the decrease in the lapse with time, as illustrated in Fig. 13 for the apparent relative velocity changes at shallow depths.

5 CONCLUSION

In this study, we investigated the sensitivity of coda waves to velocity perturbations at depth. We have presented the results from numerical wavefield simulations in media with different degrees of heterogeneity that contain a layer with perturbed velocities. We measured the apparent relative velocity changes due to the velocity perturbations at different depths. Analyses were conducted for different degrees of heterogeneity in the model, different percentages of velocity change within the layer and different times in the coda

(i) we can relate the depth sensitivity of coda waves to a combination of bulk wave sensitivity and surface wave sensitivity as described in eq. (12).

(ii) changes at depth can be detected even if the sources and sensors are placed at the free surface due to scattering that mixes surface waves and bulk waves, given a sufficiently heterogeneous medium.

(iii) from the time dependence of the relative velocity change in the coda, we can discriminate a change that occurs at the surface from a change that occurs at depth (Fig. 13).

(iv) as illustrated in Fig. 8, the apparent relative velocity changes increase linearly with the amplitude of the perturbation.

(v) in Figs 10 and 12, we demonstrate the universal behaviour of the partition ratio of bulk and surface-wave sensitivities versus the time in the coda normalized by the scattering mean free time.

We have seen that the depth sensitivity of the coda waves depends on

(i) the level of heterogeneity in the model,
(ii) the lapse time in the coda,
(iii) the degree of velocity perturbation,
(iv) the depth of the change, and
(v) the source–receiver distance.

The sensitivity kernel depends on the offset between source and receiver, nevertheless, in our geometry the sensitivity towards offsets is weak and has therefore not been addressed in more detail.

Frequency plays a crucial role in the value of the mean free time and, therefore, in the partition ratio of surface and bulk waves. Depending on the frequency band considered, the interpretation of velocity change measurements can be interpreted as the sensitivity of either body waves (Sens-Schönfelder & Wegler 2006, working at 0.5 Hz and above) or sensitivity of surface waves (Rivet *et al.* 2011, working at 0.2 Hz and below and at very early times in the coda).

An interesting observation is the importance of surface waves for shallow depth and at early times in the coda. After six mean free times, the bulk waves clearly dominate the depth sensitivity. As a general framework, we can say that at early times, the waves most probably propagate as surface waves, and are sensitive to shallow changes. Later in the coda, scattering and mode conversion have occurred and the waves sensed at the surface have spent more time in the bulk, they are therefore more sensitive to changes at depth.

This indicates the need for a precise knowledge of the scattering properties for interpreting apparent velocity changes.

These results are of interest to improve future monitoring techniques using coda waves. The results will be used, for instance, to improve the inversion schemes on real data, including the imaging and locating of small changes that occur in fault zones or volcanic areas.

ACKNOWLEDGEMENTS

This study is part of the ERC Advanced Grant Whisper 227507. We wish to thank A. Sieminski for her help with the numerical code. C. Sens-Schönfelder acknowledges a visiting grant from the University Joseph Fourier, Grenoble. We acknowledge the helpful reviews of Nori Nakata and an anonymous reviewer.

REFERENCES

Abubakirov, I.R. & Gusev, A.A., 1990. Estimation of scattering properties of lithosphere of Kamchatka based on Monte-Carlo simulations of record envelope of a near earthquake, *Phys. Earth planet. Inter.,* **64**(1), 52–67.

Aki, K. & Chouet, B., 1975. Origin of coda waves: source, attenuation and scattering effects, *J. geophys. Res.,* **80**(23), 3322–3342.

Aki, K. & Ferrazzini, V., 2000. Seismic monitoring and modeling of an active volcano for prediction, *J. geophys. Res.,* **105**(B7), 16 617–16 640.

Brenguier, F., Shapiro, N., Campillo, M., Ferrazzini, V., Duputel, Z., Coutant, O. & Nercessian, A., 2008a. Towards forecasting volcanic eruptions using seismic noise, *Nat. Geosci.,* **1,** 126–130.

Brenguier, F., Campillo, M., Hadziioannou, C., Shapiro, N.M., Nadeau, R.M. & Larose, E., 2008b. Postseismic relaxation along the San Andreas fault at Parkfield from continuous seismological observations, *Science,* **321,** 1478–1481.

Cowan, M.L., Jones, I.P., Page, J.H. & Weitz, D.A., 2002. Diffusing acoustic wave spectroscopy, *Phys. Rev. E.,* **65,** 066605, 1–11.

Derode, A., Tourin, A. & Fink, M., 2001. Random multiple scattering of ultrasound. II. Is time reversal a self-averaging process? *Phys. Rev. E.,* **64,** 066605:1–11.

Frankel, A. & Clayton, R., 1986. Finite difference simulations of seismic scattering: implications for the propagation of short-period seismic waves in the crust and models of crustal heterogeneity, *J. geophys. Res.,* **91**(B6), 6465–6489.

Grêt, A., Snieder, R., Aster, R.C. & Kyle, P.R., 2005. Monitoring rapid temporal changes in a volcano with coda-wave interferometry, *Geophys. Res. Lett.,* **32,** L06304, 1–4.

Hadziioannou, C., Larose, E., Coutant, O., Roux, P. & Campillo, M., 2009. Stability of monitoring weak changes in multiply scattering media with ambient noise correlation: laboratory experiments, *J. acoust. Soc. Am.,* **125,** 3688–3695.

Hennino, R., Trégourès, N., Shapiro, N.M., Margerin, L., Campillo, M., van Tiggelen, B.A. & Weaver, R.L., 2001. Observation of equipartition of seismic waves, *Phys. Rev. Lett.,* **86,** 3447–3450.

Holliger, K. & Levander, A.R., 1992. A stochastic view of lower crustal fabric based on evidence from the Ivrea Zone, *Geophys. Res. Lett.,* **19,** 1153–1156.

Komatitsch, D. & Vilotte, J-P., 1998. The spectral element method: an efficient tool to simulate the seismic response of 2D and 3D geological structures, *Bull. seism. Soc. Am.,* **88,** 368–392.

Larose, E., Derode, A., Clorennec, D., Margerin, L. & Campillo, M., 2005a. Passive retrieval of Rayleigh waves in disordered elastic media, *Phys. Rev. E.,* **72,** 046607, 1–10.

Larose, E., Khan, A., Nakamura, Y. & Campillo, M., 2005b. Lunar subsurface investigated from correlation of seismic noise, *Geophys. Res. Lett.,* **32,** L16201, 1–4.

Larose, E., Planès, T., Rossetto, V. & Margerin, L., 2010. Locating a small change in a multiple scattering environment, *Appl. Phys. Lett.,* **96,** 204101, 1–3.

Lobkis, O. & Weaver, R., 2003. Coda-wave interferometry in finite solids: recovery of P-to-S conversion rates in an elastodynamic billiard, *Phys. Rev. Lett.,* **90,** 254302, 1–4.

Mainsant, G., Larose, E., Brönnimann, C., Jongmans, D., Michoud, C. & Jaboyedoff, M., 2012. Ambient seismic noise monitoring of a clay landslide: toward failure prediction, *J. geophys. Res.,* **117,** F01030, doi:10.1029/2011JF002159.

Margerin, L. & Nolet, G., 2003. Multiple scattering of high-frequency seismic waves in the deep Earth: modeling and numerical examples, *J. geophys. Res.,* **108**(B5), 2234, doi:10.1029/2003JB002455.

Meunier, J., Huguet, F. & Meynier, P., 2001. Reservoir monitoring using permanent sources and vertical receiver antennae: the Céré-la-Ronde case study, *Leading Edge,* **20**(6), 622–629.

Nakata, N. & Snieder, R., 2011. Near-surface weakening in Japan after the 2011 Tohoku-Oki earthquake, *Geophys. Res. Lett.,* **38,** L17302, doi:10.1029/2011GL048800.

Niu, F., Silver, P.G., Daley, T.M., Cheng, X. & Majer, E.L., 2008. Preseismic velocity changes observed from active source monitoring at the Parkfield SAFOD drill site, *Nature,* **454,** 204–208.

Paasschens, J.C.J., 1997. Solution of the time-dependent Boltzmann equation, *Phys. Rev. E.,* **56**(1), 1135–1141.

Pacheco, C. & Snieder, R., 2005. Time-Lapse travel time change of multiply scattered acoustic waves, *J. acoust. Soc. Am.,* **118**(3), 1300–1310.

Pine, D.J., Weitz, D.A., Chaikin, P.M. & Herbolzheimer, E., 1988. Diffusing-wave spectroscopy, *Phys. Rev. Lett.,* **60,** 1134–1137.

Poupinet, G., Ellsworth, W.L. & Frechet, J., 1984. Monitoring velocity variations in the crust using earthquake doublets: an application to the Calaveras fault, California, *J. geophys. Res.,* **89**(B7), 5719–5731.

Poupinet, G., Ratdomopurbo, A. & Coutant, O., 1996. On the use of earthquake multiplets to study fractures and temporal evolution of an active volcano, *Ann. Geophys.,* **39,** 253–264.

Rivet, D., Campillo, M., Shapiro, N.M., Cruz-Atienza, V., Radiguet, M., Cotte, N. & Kostoglodov, V., 2011. Seismic evidence of nonlinear crustal deformation during a large slow slip event in Mexico, *Geophys. Res. Lett.*, **38,** L08308, 1–5.

Rossetto, V., Margerin, L., Planès, T. & Larose, E., 2011. Locating a weak change using diffuse waves: theoretical approach and inversion procedure, *J. Appl. Phys.,* **109,** 034903, 1–11.

Sato, H., 1993. Energy transportation in one- and two-dimensional scattering media: analytic solutions of the multiple isotropic scattering model, *Geophys. J. Int.,* **112,** 141–146.

Sato, H., Fehler, M. & Maeda, T., 2012. *Seismic Wave Propagation and Scattering in the Heterogeneous Earth,* Springer Verlag, Berlin-Heidelberg.

Sawazaki, K., Sato, H., Nakahara, H. & Nishimura, T., 2009. Time-lapse changes of seismic velocity in the shallow ground caused by strong ground motion shock of the 2000 western-Tottori Earthquake, Japan, as revealed from coda deconvolution analysis, *Bull. seism. Soc. Am.,* **99,** 352–366.

Sens-Schönfelder, C. & Larose, E., 2008. Temporal changes in the lunar soil from correlation of diffuse vibrations, *Phys. Rev. E.,* **78,** 045601, 1–4.

Sens-Schönfelder, C. & Larose, E., 2010. Lunar noise correlation, imaging and monitoring, *Earthq. Sci.,* **23,** 519–530.

Sens-Schönfelder, C. & Wegler, U., 2006. Passive image interferometry and seasonal variations of seismic velocities at Merapi Volcano, Indonesia, *Geophys. Res. Lett.,* **33,** L21302, doi:10.1029/2006GL0277987.

Sens-Schönfelder, C. & Wegler, U., 2011. Passive image interferometry for monitoring crustal changes with ambient seismic noise, *Comptes Rend. Geosci.,* **343,** 8–9.

Snieder, R., 2006. The theory of coda wave interferometry, *Pure appl. Geophys.,* **163,** 455–473.

Snieder, R. & Hagerty, M., 2004. Monitoring change in volcanic interiors using coda wave interferometry: application to Arenal Volcano, Costa Rica, *Geophys. Res. Lett.,* **31,** L09608, doi:10.1029/2004GL019670.

Snieder, R., Grêt, A., Douma, H. & Scales, J., 2002. Coda wave interferometry for estimating nonlinear behavior in seismic velocity, *Science,* **295,** 2253–2255.

Tatarski, V.I., 1961. *Wave Propagation in a Turbulent Medium,* McGraw-Hill, New York.

Tromp, J. & Komatitsch, D., 2008, Spectral-element and adjoint methods in seismology, *Comm. Comp. Phys.,* **3,** 1–32.

Turner, J.A., 1998, Scattering and diffusion of seismic waves, *Bull. seism. Soc. Am.,* **88**, 276–283.

Weaver, R.L., 1982. On diffuse waves in solid media, *J. acoust. Soc. Am.,* **71,** 1608–1609.

Weaver, R.L., 1985. Diffuse elastic waves at a free surface, *J. acoust. Soc. Am.,* **78,** 131–136.